PCCP

Accepted Manuscript

This is an *Accepted Manuscript*, which has been through the Royal Society of Chemistry peer review process and has been accepted for publication.

Accepted Manuscripts are published online shortly after acceptance, before technical editing, formatting and proof reading. Using this free service, authors can make their results available to the community, in citable form, before we publish the edited article. We will replace this *Accepted Manuscript* with the edited and formatted *Advance Article* as soon as it is available.

You can find more information about *Accepted Manuscripts* in the **Information for Authors**.

Please note that technical editing may introduce minor changes to the text and/or graphics, which may alter content. The journal's standard **Terms & Conditions** and the **Ethical guidelines** still apply. In no event shall the Royal Society of Chemistry be held responsible for any errors or omissions in this *Accepted Manuscript* or any consequences arising from the use of any information it contains.

www.rsc.org/pccp

Journal Name

ARTICLE

Toward enhanced hydrogen generation from water using oxygen permeating LCF membranes

Xiao-Yu Wu [a], Le Chang [a], Mruthunjaya Uddi [a], Patrick Kirchen [b], Ahmed F. Ghoniem [a],

Hydrogen production from water thermolysis can be enhanced by the use of perovskite-type mixed ionic and electronic conducting (MIEC) membranes, through which oxygen permeation is driven by a chemical potential gradient. In this work, water thermolysis experiments were performed using 0.9-mm thick $La_{0.9}Ca_{0.1}FeO_{3-\delta}$ (LCF-91) perovskite membranes at 990 ^{o}C in a lab-scale button-cell reactor. We examined the effects of the operating conditions such as the gas species concentrations and flow rates on the feed and sweep sides on the water thermolysis rate and oxygen flux. A single step reaction mechanism is proposed for surface reactions, and three-resistance permeation models are derived. Results show that water thermolysis is facilitated by the LCF-91 membrane especially when a fuel is added to the sweep gas. Increasing the gas flow rate and water concentration on the feed side or the hydrogen concentration on the sweep side enhances the hydrogen production rate. In this work, hydrogen is used as the fuel by construction, so that single-step surface reaction mechanism can be developed and water thermolysis rate parameters can be derived. Both surface reaction rate parameters for oxygen incorporation/dissociation and hydrogen-oxygen reactions are fitted at 990 ^{o}C. We compare the oxygen fluxes in water thermolysis and air separation experiments, and identify different limiting steps in the processes involving various oxygen sources and sweep gases for this 0.9 mm thick LCF-91 membrane. In the air feed-inert sweep case, the bulk diffusion and sweep side surface reaction are the two limiting steps. In the water feed-inert sweep case, surface reaction on the feed side dominates the oxygen permeation process. Yet in the water feed-fuel sweep case, surface reactions on both the feed and sweep sides are rate determining when hydrogen concentration in the sweep side is in the range of 1 - 5 vol%. Furthermore, long term studies show that the surface morphology changes and silica impurities have little impact on the oxygen flux for either water thermolysis or air separation.

1. Introduction

The continuous rise of CO_2 emission and its accumulation in the atmosphere have been shown to contribute to global warming. According to IEA, CO_2 emission is expected to keep increasing in the next two decades, and its rate will double by 2030 from its value in 1990 based on the policies in 2012 [1]. Efforts are under way to decrease CO_2 emission by expanding the use of renewables, improving generation and end use efficiency, switching to low carbon fuels, etc.

Power generation from fossil fuel is one of the major sources of CO_2 emission, and several major approaches have been proposed to capture CO_2 from fossil fuel power generation processes [2]. Efficient production of hydrogen from water is another way to decrease CO_2 emission, because combustion of hydrogen doesn't produce CO_2 and hydrogen can be utilized in power generation and transportation systems with higher thermodynamic efficiency such as fuel cells. Several

applications have been proposed for hydrogen production from water, such as electrolysis, photoelectrolysis and thermolysis. So far, electrolysis is still the only approach that can be economically utilized to produce hydrogen from water.

Studies have been carried out to optimize the components in electrolysis systems to increase the efficiency and stability (see [3,4,5] and reference therein). Yet water electrolysis consumes a high quality energy source, i.e., electricity, and the operating cost is still high. From DOE analysis, the costs for current central grid electrolysis and PEM (polymer electrolyte membrane) electrolysis are \$4.14/kg-H_2 [6] and \$5.12/kg-H_2 [7], respectively, which are more than twice of the cost for natural gas reforming plants (\$1.7/kg-H_2 [8]). Yet natural gas reforming plants produce significant amount of CO_2 and consumes non-renewables in the hydrogen production process. In order to decrease the cost of H_2 production from water, processes that utilize heat and/or chemical potential to drive the water splitting

process is needed. Water thermolysis can be enhanced by removing one of the products; an alternative is driven by chemical potential. Water thermolysis on mixed ionic-electronic conductive (MIEC) membranes with oxygen permeability have been demonstrated [9,10,11,12,13,14,15,16]. For a water thermolysis membrane reactor, there are no moving components or electronic circuits; therefore, less maintenance is expected compared to electrolysis or chemical looping systems. Yet life-cycle economic analysis should be carried out to compare these systems in further studies.

Perovskite, whose chemical formula is ABO_3, has been studied extensively as catalysts, oxygen ion and electron conductive materials. By varying the cations and/or adding dopants, a subset of perovskite exhibits both ionic and electronic conductivities at elevated temperature. When exposed to oxygen partial pressure gradient, the MIEC perovskite is oxygen selective-permeable. The oxygen diffusion capabilities in perovskite materials are attributed to the existence of oxygen vacancies and the mobility of charged species, i.e., electrons, holes, lattice oxygen and oxygen vacancies. Different cation combinations or dopants have been explored to enhance oxygen permeability of perovskite for oxygen separation and hydrogen production (see [17,18,19] and reference therein).

Extensive work has been published on constructing better MIEC perovskite materials for oxygen separation. For membranes with thickness around 1 mm, reported oxygen fluxes at 800 – 1000 °C are in the range of 0.01 – 5 μmol/cm^2-s [19]. Transition metals, i.e., Fe, Co and Mn, are usually doped into the cations to increase the oxygen defects and increase the oxygen permeation rate. Aasland et al. [20] investigated the oxygen permeation through a 1 mm $SrFe_{0.67}Co_{0.33}O_{3-\delta}$ membrane at 1000 °C, measuring the oxygen flux as high as 2.06 μmol/cm^2-s using helium as the sweep gas. However, new phases were found on the surface of the used membranes. More recently, Liao et al. [21] published a study on the 1 mm thick $BaBi_{0.05}Co_{0.8}Ta_{0.15}O_{3-\delta}$ membranes and found that oxygen flux reached 1.86 μmol/cm^2-s with air feed and helium sweep.

Only few studies have analyzed the results of oxygen permeation from other oxygen-containing molecules such as water and carbon dioxide. When water serves as the oxygen source, its thermolysis occurs on the membrane surface and hydrogen can be produced. The concept has been demonstrated using different MIEC perovskite membranes, i.e., $La_{0.6}Sr_{0.4}Co_{0.2}Fe_{0.8}O_{3-\delta}$ [11], $SrCo_{0.4}Fe_{0.5}Zr_{0.1}O_{3-\delta}$ [13], $BaCo_xFe_yZr_{1-x-y}O_{3-\delta}$ [15] and $La_{0.7}Sr_{0.3}Cu_{0.2}Fe_{0.8}O_{3-\delta}$ [22], but the mechanism is not well understood. Most of the studies used fuel, such as hydrogen and carbon monoxide to facilitate oxygen permeation through the membrane; as a result, oxygen fluxes in the range of 0.02 – 3.5 μmol/cm^2-s were reported. Yet few studies used inert sweep gases. Catalysts, such as Pt were also applied to improve water thermolysis on the feed side and hence increasing the oxygen flux and hydrogen production rate [23].

The mechanism for water thermolysis coupled with oxygen permeation through an MIEC perovskite membrane is far more complicated than oxygen permeation from air. Water thermolysis produces hydrogen on the feed side, and that hydrogen needs to be removed from the membrane surface to enable the reaction to continue. Heterogeneous reactions on the membrane surface as well as electron transfer between solid and gas species contribute to the mechanism. Careful studies are needed in order to examine the oxygen diffusion mechanism with water thermolysis on MIEC membranes.

Using different oxygen sources, e.g., air vs. water, the limiting step(s) of the oxygen permeation, either surface reactions or bulk diffusion, may be different. Few studies have compared these two options using the same membrane materials and under the same operating conditions. Besides, the stability of perovskite materials with either air or water vapor as oxygen source is also of interest. In this paper, careful experiments were performed on dense $La_{0.9}Ca_{0.1}FeO_{3-\delta}$ (LCF-91) perovskite membranes with different oxygen sources and sweep gases. Although LCF has lower oxygen flux than other popular oxygen permeable perovskite membranes [24], this material is chosen for the following reasons. First, LCF-91 is stable in helium, CO_2, H_2 and CH_4 sweep conditions [25]. It is desired to incorporate syngas production from partial oxidation of hydrocarbons on the sweep side to enhance oxygen permeation in the future work, so the stability of the materials in $CH_4/CO_2/CO/H_2$ environment is important in practice. Besides, as discussed later in the paper, the bulk diffusion is not the limiting step when water is oxygen source at high temperature, which enables us to study the heterogeneous water thermolysis on the LCF-91 membrane even though the oxygen diffusivity is not high. As to the reactive sweep gas, hydrogen-helium mixture is used by construction, because the reaction on the sweep side is the reverse water thermolysis on the feed side, which enables us to derive the reaction rate constants for heterogeneous water thermolysis. The understanding of the heterogeneous mechanism built the bases for further studies to incorporate hydrocarbon oxidation in the sweep side, which has been found to enhance oxygen permeation [26]. With these considerations, we performed careful experiments and demonstrate that water thermolysis can be enhanced using a dense 0.9-mm thick LCF-91 perovskite membrane with either inert or reactive sweep gas. Besides, oxygen permeation results of both water vapor and air as oxygen sources are shown; mechanism is quantified and compared. The effects of feed and sweep gases species, concentrations and flow rates are investigated and the limiting step(s) for oxygen permeation from air or water vapor are reported.

2. Experiments

2.1 Experimental setup

A button-cell membrane reactor with axis-symmetric stagnation flow field is designed for the oxygen permeation experiments

with various oxygen sources. The reactor is shown in Figure 1. It is constructed of alumina and can operate at temperatures up to 1050 °C at atmospheric pressure. Inside the reactor, a flat circular perovskite membrane with an effective diameter of 12.7 mm is installed between the two outside alumina tubes. Two gold rings are used to seal the gap between the membrane edges and the tubes, and a spring is installed at the top to enforce the sealing by a downward force. The reactor is divided into a feed chamber (high p_{O2}) and a sweep chamber (low p_{O2}). The reactor is installed inside a furnace, which has an electric heater with PID controller and a K-type thermocouple feedback to control the temperature ramp rate of 3°C/min for both heating and cooling during all experiments. The small temperature ramp rate ensures low thermal stress within the membrane, gold sealant and reactor. Additionally, each chamber has a K-type thermocouple in a position as close as possible to the surface to measure the temperature on both sides. The distance from the thermocouple tip to the membrane is measured, and the membrane temperature is calculated by linear interpolation of the two temperatures. The furnace temperature is controlled to maintain the set reactor temperature, i.e. 990 °C in this study.
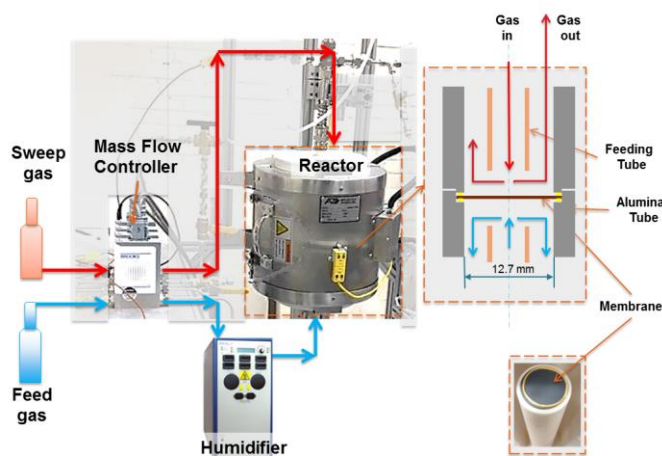

Figure 1. Schematic flow chart shows a button-cell reactor. The effective diameter of the membrane is 12.7 mm. For air feed experiments, the humidifier is by-passed; dry air is fed into the reactor. For water thermolysis experiments, inert gas flows through the humidifier to carry desired amount of water vapor into reactor

Gases are supplied into the feed and sweep chambers from high pressure gas cylinders, and the flow rates are controlled by MFCs (mass flow controller) from Brooks Instrument®. In order to precisely control the flow rate, only one type of gas flows through an MFC at one time; therefore, multiple MFCs are installed at both feed and sweep inlets to obtain desired gas mixtures. During the water thermolysis experiments, argon is used as the carrier gas, which goes through a humidifier (Fideris® Bubble Humidifier) to carry desired amount of water vapor into the feed side chamber; both the water bath and dew

point temperatures of the humidifier can be controlled to maintain the desired water partial pressures. For the experiments with air as the oxygen source, the humidifier is by-passed and dry air is fed into the reactor. Alumina feeding tubes were inserted into both chambers in the reactor to lead the gases towards the membrane surfaces; the feeding tubes with 4.75 mm ID and 6.35 mm OD were used.

Gas samples, both at the inlet and outlet of feed and sweep chambers, are examined by the GCs (gas chromatograph, Agilent 490 Micro GC and Shimadzu GC2014), where the concentrations of different gases are measured and printed. The Micro GC has a 10 m 5 Å molecular sieve column (helium carrier gas) with TCD detectors to measure hydrogen, oxygen and nitrogen concentrations, and the Shimadzu GC2014 has a PDHID detector to detect hydrogen concentration at ppm levels. Careful calibrations were made to the GCs, and the two-point interpolation method was used for the measurements. These well-mixed bulk values at the inlets and outlets of the membrane reactor describe the overall reaction and performances inside the reactor.

2.2 LCF membrane

The perovskite membrane tested in this paper is 0.9 mm thick $La_{0.9}Ca_{0.1}FeO_{3-\delta}$ (LCF-91) dense membranes provided by Ceramatec. Ca-substitution in the La site of $LaFeO_3$ (LFO) lattice leads to charge compensation by either forming oxygen vacancies or oxidizing Fe^{3+} to Fe^{4+}, hence, decreasing oxygen permeation barriers [27]. However, as Ca is substituted, phase separation might occur, which leads to a mixture of perovskite ($La_{1-x}Ca_xFeO_3$), Grenier ($LaCa_2Fe_3O_8$) and brownmillerite ($Ca_2Fe_2O_5$) phases [28]. The Goldschmidt tolerance factor, T_G, is often used to identify whether the chemical compound can form a stable perovskite lattice, and the tolerance factor for $La_xCa_{1-x}FeO_{3-\delta}$ can be calculated as

$$T_G = \frac{xr_{La} + (1-x)r_{Ca} + r_O}{\sqrt{2}\left(r_{Fe} + r_O\right)} \quad (1)$$

in which, r_i is the radius of the i ion. For LCF, radii of the ions are [29]: La^{3+}: 1.36 Å, Ca^{2+}: 1.34 Å, Fe^{3+}: 0.55 Å (low spin) & 0.645 Å (high spin), Fe^{4+}: 0.585 Å, O^{2+}: 1.40 Å. As the concentration of Fe^{3+} and Fe^{4+} varies at different oxygen vacancy concentrations, the tolerance factor T_G reaches the maximum when all iron ions are at Fe^{3+} low spin state and it reaches the minimum when all iron ions are at Fe^{3+} high spin state. Therefore, LCF-91 has a tolerance factor in the range of $0.954 < T_G < 1.00$, indicating that at least the material LCF-91 is in a stable perovskite structure.

Under operating conditions such as high temperature and reducing gases, new phases or element segregations may occur on the perovskite surface. Hence, in this study, the membranes were characterized both before and after experiments to identify whether phase change and segregation occurred. Scanning electron microscopy (SEM) and energy-dispersive X-ray

spectroscopy (EDX) were carried out on JEOL 5910 General Purpose SEM. X-ray powder diffraction (XRD) patterns were obtained from PANalytical X'Pert Pro Multipurpose Diffractometer with nickel filtered copper source with X'Celerator detector. EDX results for membranes before experiments are shown in Table 1, from which we can see that the concentration of cations matches the ideal LCF-91 stoichiometry. The XRD data of LCF-91 membrane before the experiments only shows the perovskite peak as later shown later in Section 7.2. That means the original LCF-91 membrane has only one perovskite phase.

Table 1 Quantitative EDX results show the stoichiometry of the LCF-91 membrane materials

|	Elements	La	Ca	Fe
New membrane	Atomic concentration* (%)	42.41 ±1.16	5.53 ±0.56	52.06 ±1.24
	Calculated stoichiometry	0.885 ±0.023	0.115 ±0.011	1.09 ±0.025

* Only cations are counted: $X_{La} + X_{Ca} + X_{Fe} = 1$

3. Data deduction

As discussed above, during water thermolysis experiments, the hydrogen concentration at the outlet of the feed chamber is measured by the gas chromatograph. The homogeneous reaction of water thermolysis is slow even at elevated temperature around 990 ^{o}C, so in the analysis, the homogeneous reaction of water thermolysis is ignored and only heterogeneous reaction is considered. Therefore, the hydrogen production rate (yield), Y_{H_2}, is be calculated as

$$Y_{H_2} = X'_{H_2,out} \times n' \quad (2)$$

where $X'_{H_2,out}$ is the hydrogen molar concentration at the outlet of the feed side and n' is total molar flow rate, mol/s. The water thermolysis reaction (3) shows that the total molar flow rate of the feed gas mixture does not change,

$$H_2O + V_O^{\bullet\bullet} \leftrightarrow O_O^x + 2h^\bullet + H_2 . \quad (3)$$
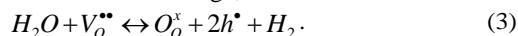
Due to the low water thermolysis ratio, the water concentration inside the reactor can be assumed to the same as that at the inlet $X'_{H_2O,in}$. Therefore, the total molar flow rate on the feed side is

$$n' = n'_{Ar} + n'_{H_2O} = \frac{n'_{Ar}}{1 - X'_{H_2O,in}} . \quad (4)$$

Besides, the hydrogen concentration $X'_{H_2,meas}$ is measured in the dry gas after passing the drier, which is not the same with that at the outlet of the reactor, $X'_{H_2,out}$. Yet they are related by the relation

$$X'_{H_2,out} = \frac{X'_{H_2,meas} \cdot n'_{Ar}}{n'} = X'_{H_2,meas} \cdot (1 - X'_{H_2O,in}) . \quad (5)$$

Combining Equations (2), (4) and (5), we have

$$Y_{H_2} = X'_{H_2,meas} \times n'_{Ar} . \quad (6)$$

Then the water thermolysis ratio is defined as

$$R'_{H_2O} = \frac{Y_{H_2}}{n'_{H_2O}} = \frac{Y_{H_2}}{n'_{Ar} \cdot \dfrac{X'_{H_2O,in}}{1 - X'_{H_2O,in}}} . \quad (7)$$

Besides, as the water thermolysis rate is low, we assume that all the oxygen produced from water thermolysis diffuses through the membrane. Hence, the oxygen flux is related to the hydrogen yield, as

$$J_{O_2} = \frac{Y_{O_O^x}/2}{A_{memb}} = \frac{Y_{H_2}}{2A_{memb}} \quad (8)$$

where $Y_{O_O^x}$ is the lattice oxygen yield from Equation (3).

In the case when a mixture of hydrogen and helium acts as the sweep gas, the hydrogen consumption ratio on the sweep side is

$$R''_{H_2} = \frac{Y_{O_O^x}}{n''_{H_2,in}} = \frac{Y_{H_2}}{X''_{H_2,in} n''} \quad (9)$$

where the $X''_{H_2O,in}$ is the hydrogen concentration of the fuel mixture at the sweep side inlet, and n'' is the total molar flow rate on the sweep side.

We also measured the oxygen fluxes when air was used as the feed gas for comparison. For the air feed-inert sweep case, the absolute amount of oxygen that diffuses through the membrane is calculated by excluding the air leakage into the sweep side. The air leakage is tracked from the nitrogen concentration by assuming that oxygen and nitrogen molar ratio in air leakage is 21:79. Nitrogen and oxygen atom balance as well as the overall molar balance (no reaction between gases) are as
Oxygen balance:

$$\dot{n}''_{t,in} X''_{O_2,in} + \dot{n}_{O_2} + 0.21\dot{n}_{leak} = \dot{n}''_{t,out} X''_{O_2,out} \quad (10)$$

Nitrogen balance: $0.79\dot{n}_{leak} = \dot{n}''_{t,out} X''_{N_2,out} \quad (11)$

Overall balance: $\dot{n}''_{t,in} + \dot{n}_{O_2} + \dot{n}_{leak} = \dot{n}''_{t,out} \quad (12)$

where $\dot{n}''_{t,in}$ and $\dot{n}''_{t,out}$ are the molar flux at the inlet and outlet of the sweep chamber, respectively; $\dot{n}_{O_2}$ is the oxygen molar flux through the membrane; $\dot{n}_{leak}$ is the molar flux of the air leakage; $X''_{i,in}$ and $X''_{i,out}$ are the molar concentrations of species i at inlet and outlet of the sweep chamber, respectively.

At the inlet, as high purity helium gas flows into the reactor, the oxygen concentration is zero, i.e., $X''_{O_2,in} = 0$. From Equations (10), (11) and (12), we can calculate the oxygen flux and leak flux as:

$$\dot{n}_{O_2} = \frac{\left(X''_{O_2,out} - \dfrac{0.21}{0.79} X''_{N_2,out} \right)}{1 - X''_{O_2,out} - X''_{N_2,out}} \dot{n}''_{t,in} \quad (13)$$

$$\dot{n}_{leak} = \frac{X''_{N_2,out}/0.79}{1 - X''_{O_2,out} - X''_{N_2,out}} \dot{n}''_{t,in} \quad (14)$$

Then the oxygen flux is

$$J_{O_2} = \dot{n}_{O_2} / A_{memb} \quad (15)$$

where A_{memb} is the effective area of membrane surface.

For the air feed-fuel sweep case, the oxygen fluxes can be calculated from either oxygen permeation on the feed side or hydrogen consumption on sweep side. From oxygen permeation (the feed side), we have

Oxygen balance: $\dot{n}'_{t,in} X'_{O_2,in} - \dot{n}'_{t,out} X'_{O_2,out} = \dot{n}_{O_2}$ (16)

Overall balance: $\dot{n}'_{t,in} - \dot{n}'_{t,out} = \dot{n}_{O_2}$ (17)

Therefore, from the above balance equations, the oxygen flux is

$$j_{O_2} = \frac{\dot{n}_{O_2}}{A_{memb}} = \frac{\dot{n}'_{t,in}\left(X'_{O_2,in} - X'_{O_2,out}\right)}{A_{memb}\left(1 - X'_{O_2,out}\right)}$$ (18)

On the other hand, as hardly any oxygen was detected in the sweep side when hydrogen is used as a sweep gas, we assume that all the oxygen permeated through the membrane reacts with the hydrogen. As $H_2 + 1/2 O_2 \leftrightarrow H_2O$, the permeated oxygen won't change the total molar flux of the gas mixture, which leads to

$$\dot{n}''_{t,in} = \dot{n}''_{t,out} = \dot{n}''_t$$ (19)

Therefore, the oxygen flux equals half of the hydrogen consumption rate in the sweep side, which is

$$J_{O_2} = \frac{\left(X''_{H_2,in} - X''_{H_2,out}\right) \times \dot{n}''_t}{2 A_{memb}}$$ (20)

The oxygen fluxes calculated from Equations (18) and (20) are compared to verify the mass balance in the reactor.

And for all the cases, the residence time inside the reactor is estimated as

$$\tau = \frac{V}{Q} = \frac{\pi d_r^2 L}{4} \frac{T_s}{Q_s T_r}$$ (21)

where V is the volume of the reactor, Q is the volumetric flow rate, d_r is the inner diameter of the reactor, L is the length of the reactor inside the furnace, T_s is the standard temperature, Q_s is the standard volumetric flow rate and T_r is the temperature in the reactor.

4. Water thermolysis on MIEC membrane

Molecules that contain oxygen atoms may theoretically serves as the oxygen source for the permeation process through an MIEC membrane. When water serves as the oxygen source, a water thermolysis reaction takes place on the feed side (high p_{O_2}); on the sweep side (low p_{O_2}), the permeated oxygen is carried away by an inert gas or consumed by fuel mixtures. Both homogeneous and heterogeneous water thermolysis may take place. However, homogeneous water dissociation in the gas phase is a very slow process with low thermodynamic equilibrium constants even at temperatures as high as 990 °C. We calculated the thermodynamic equilibrium and the kinetic process using Cantera [30], and GRI-Mech 3.0 mechanism [31] was implemented to resolve the gas phase reactions. Results are shown in Figure 2. At 990 °C, the equilibrium hydrogen molar

fraction varies from 1 to 16 ppm as water concentration in the initial H_2O+Ar mixture increases from 1 vol% to 100 vol%. When the initial water concentration is higher than 50 vol%, the increase of equilibrium hydrogen molar fraction slows down. Therefore, initial water concentration at 50 vol% is chosen as the base case to compare with the experimental data, with hydrogen concentration being 10.1 ppm at equilibrium. Furthermore, Figure 2 (b) shows the evolution of molar fractions in a well stirred reactor for homogeneous water thermolysis at 990 °C with initial water concentration to be 50 vol%. Homogeneous thermolysis is very slow even at 990 °C: it takes about 1100 s for the gas mixture to reach 90% of the equilibrium values, and 512 s to reach 50%.

In this section, we show that water thermolysis process can be enhanced by the oxygen permeating LCF-91 membranes. Experiments were carried out to demonstrate the effect of different parameters such as feed and sweep side flow rates, feed side water concentration and fuel concentration on the sweep side. For each operating condition, we waited for the equilibrium of the reactor and then recorded the temperatures and species concentrations from successive measurements (at least five).
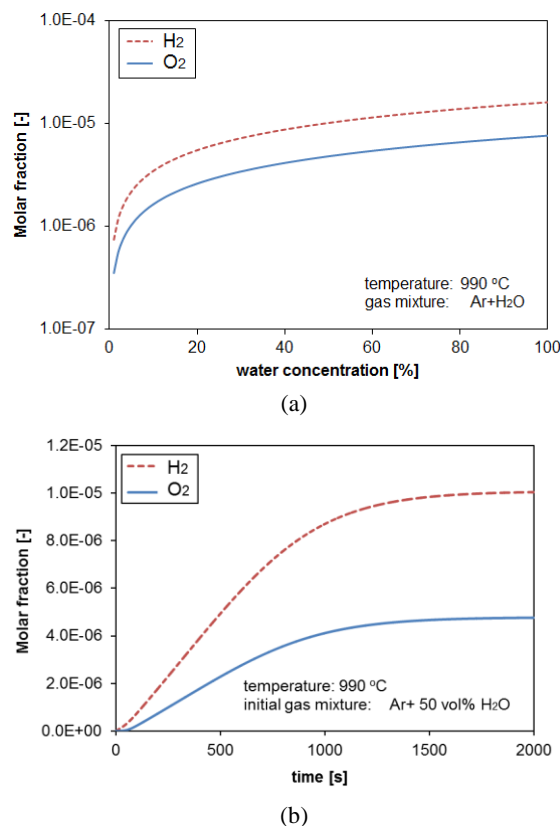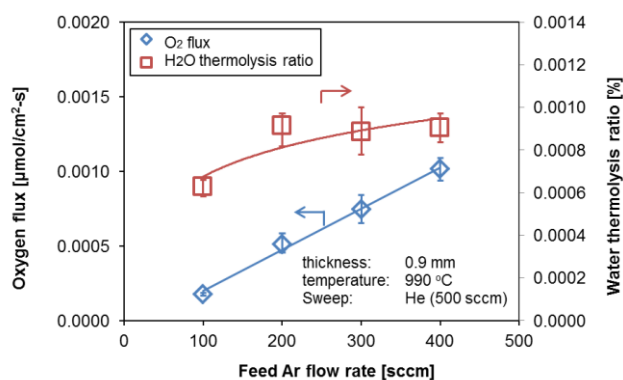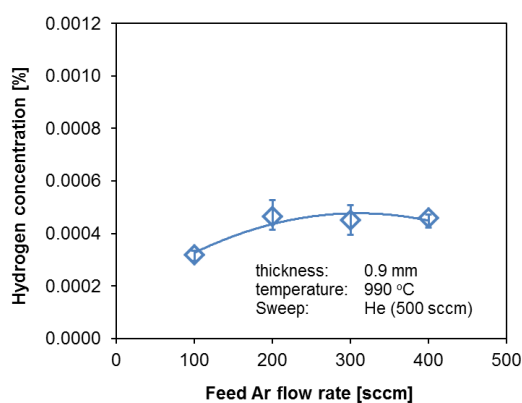

(a)

(b)

Figure 2 Homogeneous water thermolysis (a) Water concentration in the mixture affects the equilibrium hydrogen and oxygen molar fractions in the mixtures at 990 °C; (b) the species concentrations, i.e., X_{H_2} and X_{O_2} evolve with time under the initial condition of Ar and 50 vol% water mixture at 990 °C

Besides, LCF-91 membranes with the same thickness but from different batches were examined. Most of the measured values were averaged over data sets from at least two different 0.9-mm thick LCF-91 membranes in order to eliminate the effects of membrane preparations. The mean values of each dataset are presented with error bars representing the range of values due to experimental uncertainties and different LCF-91 membranes. Hydrogen is used as the fuel on sweep side to enhance water thermolysis rate. As discussed before, hydrogen is chosen in part in order to model the reverse water thermolysis using the permeation model as discussed later. In order to exclude the leakages of hydrogen from sweep to feed chambers, we measured the leakage under the conditions where feed and sweep flow rates were the same but the feed gas was a dry inert gas. In this way, the hydrogen leakage into the feed side could be quantified and the absolute amount of hydrogen produced from water thermolysis derived.

(a)

(b)

Figure 3 Water splitting rate on feed side increases with the carrier gas, i.e., argon flow rate. Yet the water thermolysis ratio (a) and hydrogen concentration (b) reaches a plateau at argon flow rate higher than 200 sccm. Feed side water concentration is fixed at 50 vol.%

4.1 Mixture flow rate on feed side

During the water thermolysis reaction on the feed side, the hydrogen-oxygen bonds break either on the membrane surface

(heterogeneously) or in the gas phase (homogeneously). Next, the hydrogen radicals recombine into hydrogen molecules that are carried away by the feed gas. Meanwhile, oxygen radicals occupy the vacancies and incorporate to form lattice oxygen. In order to study how the mixture flow rates on feed side affect the hydrogen yield, we examined the water thermolysis rate and hydrogen yield by varying the argon carrier gas flow rate while fixing the water concentration at 50.7 vol% (the corresponding dew point temperature is 82 ^{o}C in the humidifier) and membrane temperature at 990 ^{o}C. Results are shown in Figure 3 (a); higher feed rate leads to higher oxygen flux. However, with increasing feed flow rate, the water thermolysis ratio at the outlet on the feed side increases first and then reaches a plateau. The same trend is observed with the hydrogen concentration on the feed side. As shown in Figure 3 (b), the hydrogen concentration on the feed side increases as the feed flow rate increases from 100 to 200 sccm; after that, the hydrogen concentration saturates.

Increasing the gas flow rate on the feed side increases the mass transfer rate in the gas phase. Moreover, the recirculation zone size at the membrane corner is reduced as the flow rate increases, leading to smaller mass transfer resistance. As a result, at higher flow rate the hydrogen produced from water thermolysis can be convected away from the feed side membrane surface more effectively, and the hydrogen concentration at the membrane surface decreases. Additionally, the residence time in the reactor is in the order of magnitude around 0.01s, and yet the hydrogen concentration measured at the exit of the reactor is about half of the homogeneous equilibrium case which could be achieved in 512 s in homogeneous water thermolysis reaction. Due to mass transfer in gas phase, the hydrogen concentration at the membrane surface where heterogeneous reaction takes place can be higher than the concentration at the exit. Therefore, we can conclude that water thermolysis rate is enhanced on the LCF-91 membrane.

4.2 Feed water concentration

The water concentration on the feed side also affects the oxygen permeation rate and the water thermolysis rate. During the experiments, we fixed the argon carrier gas flow rate at 400 sccm while changing the water concentration in the gas mixture from 50.7 to 83.5 vol% by varying the dew point temperature of the humidifier from 82 to 95 ^{o}C. When the water concentration increases, the total flow rate of the feed gas mixture increases because the argon carrier gas has a constant flow rate of 400 sccm.

Figure 4 (a) shows that the oxygen flux has a three-fold increase when water partial pressure increases from 0.507 atm to 0.835 atm. As increasing the water concentration drives the forward reaction of water thermolysis further (Equation (3)), the hydrogen production rate or oxygen permeation rate increases. However, the water thermolysis ratio decreases by

30% percent with increasing water concentration from 50.7 to 83.5 vol%. On the other hand, the hydrogen concentration on the feed side doesn't change much with increasing water concentration, as shown in Figure 4 (b). When water concentration increases, the hydrogen concentration at the exit of the reactor remains around 0.0005%. Together with Equation (7), this explains why the water thermolysis ratio decreases with increasing water concentration.
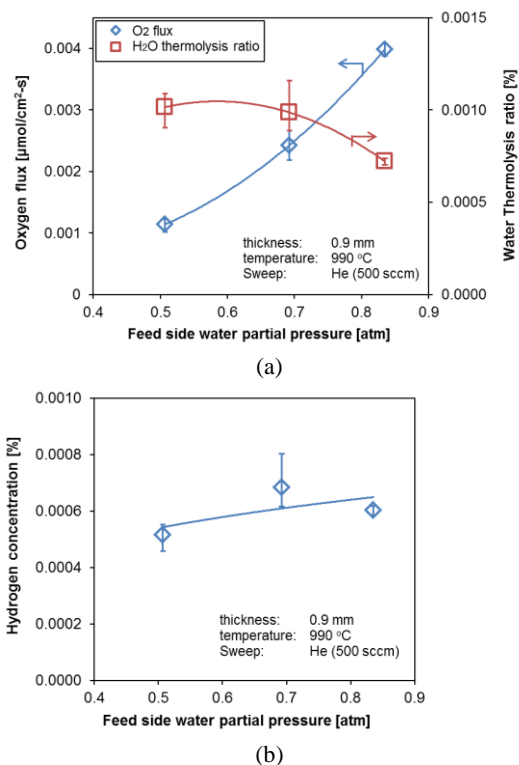

(a)

(b)

Figure 4 With increasing water concentration, (a) the oxygen fluxes increases, but the water thermolysis ratio decreases; and (b) the hydrogen concentration at feed side keeps constant.

4.3 Helium sweep gas flow rate

In order to examine the impact of the inert gas flow rate on the sweep side on the overall oxygen permeation, helium sweep gas flow rates varying in the range of 130 – 3000 sccm were tested on a 0.9 mm thick membrane at 990 ^{o}C. The feed side condition was fixed: the argon carrier gas flows at 400 sccm and the water partial pressure is 0.507 atm. Results shown in Figure 5 indicate that the oxygen flux has no obvious dependence on the helium sweep rate, and the flux is around 1.0E-3 μmol/cm^2-s. The same trend is observed for the water thermolysis ratio, which remains at around 0.001% in all the cases.
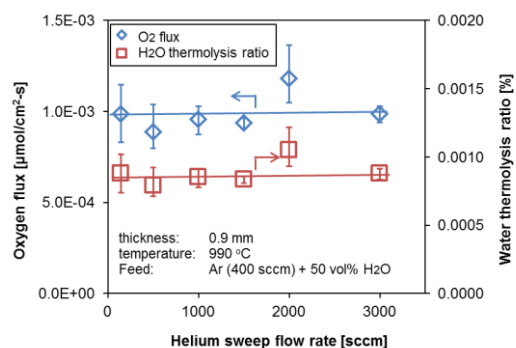

Figure 5 The oxygen fluxes and water thermolysis ratio don't change with increasing helium sweep gas flow rate

Sweep gas carries away the oxygen desorbed from the membrane surface. Higher flow rate leads to higher convective mass transport away from the membrane. This also increases the oxygen desorption rate on the sweep side as the local oxygen concentration decreases. The very weak dependence of the oxygen flux on the sweep flow rate means that the oxygen permeation process depends very weakly on the oxygen desorption process on the sweep side for this 0.9 mm LCF-91 membrane. The limiting step(s) on this case will be further discussed later in this paper.
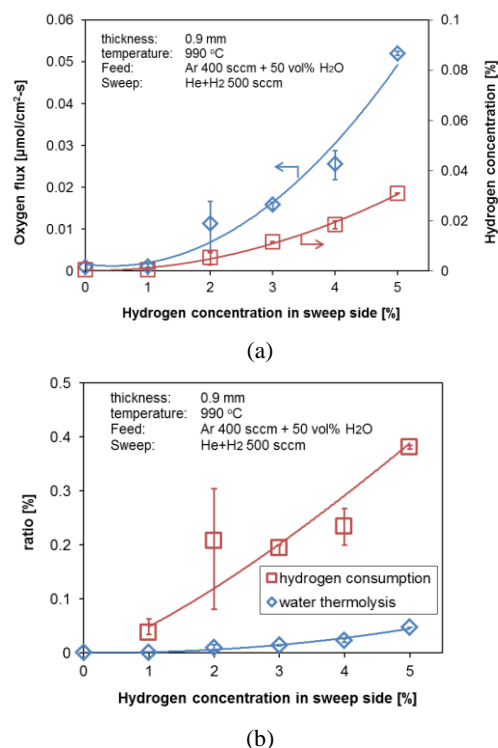

(a)

(b)

Figure 6 With increasing hydrogen concentrations on the sweep side, (a) oxygen fluxes and hydrogen concentration on the feed side as well as (b) hydrogen consumption ratio on the sweep side and water thermolysis ratio on the feed side all increase

4.4 Fuel concentration in sweep gas mixture

Because the helium sweep flow rate has hardly any effects on the water thermolysis rate, we tried another way to maintain low oxygen chemical potential in the sweep chamber, which is to add reactive gases to the sweep gas. In this case, the sweep flow not only carries away the oxygen permeated through the membrane but also reacts with it to further enhance the oxygen chemical potential gradient across the membrane. Hydrogen addition into the sweep gas is found to enhance the oxygen fluxes, as shown in Figure 6. The use of hydrogen is by construction in order to derive the water thermolysis reaction parameters shown later in this paper. As discussed above, the hydrogen leakage into the feed side is quantified at the operating conditions and the absolute hydrogen production rate is calculated by excluding the leakage into the feed side. The sweep gas mixture flows at a fixed flow rate of 500 sccm while varying the hydrogen concentrations in the sweep gas. The argon carrier gas flows at 400 sccm on the feed side, and 50.7 vol% H_2O exists in the feed gas mixtures. As shown in Figure 6 (a), the oxygen flux and hydrogen concentration on the feed side increase with the fuel concentration in the sweep gas. When 5 vol% hydrogen is added, the oxygen flux reaches 0.052 $\mu mol/cm^2$-s, more than 50 times higher than the pure helium sweep case.

Additionally, the thermolysis rate also increases with the hydrogen concentration on the sweep side, as shown in Figure 6 (b). In the same figure, we can see that the hydrogen consumption ratio on the sweep side also increases. Thus, the addition of a fuel in the sweep gas mixture is very important for increasing the water thermolysis rate and the effectiveness of the overall process. However, the stability of the membrane material in a highly reducing environment should be studied. Besides, it is undesirable to use hydrogen as a fuel to enhance water thermolysis. Therefore, further experiments on the use of hydrocarbons as fuel will be carried out.

5. Reaction kinetics for oxygen permeation

In the previous section, results show that LCF-91 membrane is capable of facilitating water thermolysis reaction with either inert or fuel sweep gases at 990 ^{o}C. Hydrogen production is the main purpose of water thermolysis; and the hydrogen production is related with the oxygen flux through the membrane by

$$J_{H_2} = 2J_{O_2}. \qquad (22)$$

In order to examine the mechanism of water thermolysis, we also carried out oxygen permeation experiments using air as the oxygen source in the same reactor at 990 ^{o}C. The oxygen fluxes under various operating conditions are compared. In this section, we first develop a mechanistic model for the oxygen permeation process under various conditions. Next we derive the kinetic parameters for the associated surface reactions.

5.1 Resistance model

The oxygen permeation process through an MIEC membrane can be divided into five steps: two mass transfer steps between gas phase and the surface, two surface reaction steps and a bulk diffusion step through the membrane. Depending on the reactor configuration, temperature and membrane thickness, any of the five steps could be rate-limiting. The two mass transfer processes in the gas phase depend on the flow rate and mass diffusion coefficients. The other three processes involving the gas/solid reactions are characteristics of the membrane material and can be modelled as a resistance network, as shown in Figure 7. The three-resistance permeation model has been used in literature to describe the oxygen permeation in cases where air is used as an oxygen source and inert gas is used to sweep [32] [33] [34] [35].
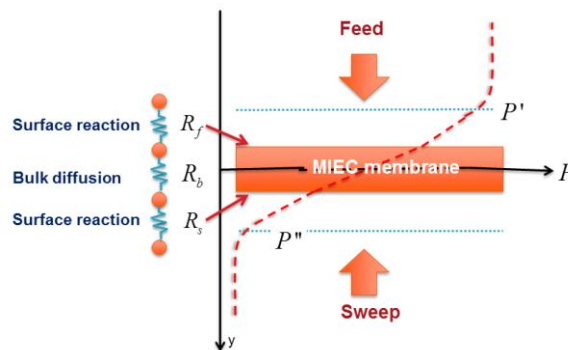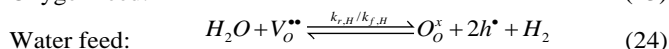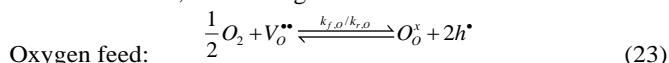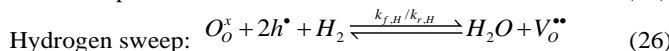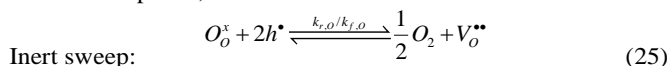

Figure 7 Three-resistance model for oxygen permeation through an inorganic membrane is illustrated. Feed and sweep sides are with high and low potential, *P'* and *P''*, respectively

In this study, the oxygen source is either air or water carried into the reactor by inert carrier gas, and the sweep gas is either inert or reactive. Therefore, oxygen incorporation/dissociation reaction or the forward/reverse water thermolysis reaction takes place. Assuming one-step heterogeneous reaction between the gas phase and the solid membrane surface, we derive the following reaction equations.
On the feed side, the heterogeneous surface reactions are:

Oxygen feed:
$$\frac{1}{2}O_2 + V_O^{\bullet\bullet} \xrightleftharpoons[k_{r,o}]{k_{f,o}} O_O^x + 2h^\bullet \qquad (23)$$

Water feed:
$$H_2O + V_O^{\bullet\bullet} \xrightleftharpoons[k_{f,H}]{k_{r,H}} O_O^x + 2h^\bullet + H_2 \qquad (24)$$

On the sweep side, the reactions are:

Inert sweep:
$$O_O^x + 2h^\bullet \xrightleftharpoons[k_{f,o}]{k_{r,o}} \frac{1}{2}O_2 + V_O^{\bullet\bullet} \qquad (25)$$

Hydrogen sweep:
$$O_O^x + 2h^\bullet + H_2 \xrightleftharpoons[k_{r,H}]{k_{f,H}} H_2O + V_O^{\bullet\bullet} \qquad (26)$$

Here, $V_O^{\bullet\bullet}$ is oxygen vacancy in LCF-91 lattice, $h^\bullet$ is the electron holes. $k_{f,o}$ and $k_{r,o}$ are the forward and reverse reaction rate constants for oxygen incorporation reaction (23), respectively, while $k_{f,H}$ and $k_{r,H}$ are the forward and reverse reaction rate constants for hydrogen oxidation reaction (26), respectively. Note that reactions (24) and (25) are the backward reactions of (26) and (23).

From the surface reactions (23) - (26), we can derive the absolute oxygen vacancy fluxes at the surface under various conditions as:

Oxygen feed side:
$$J'_V = k_{f,O} C'^{0.5}_{O_2} C'_V - k_{r,O} C'_{O_O^x} C'^2_{h^\bullet} \qquad (27)$$

Water feed side:
$$J'_V = k_{r,H} C'_{H_2O} C'_V - k_{f,H} C'_{O_O^x} C'^2_{h^\bullet} C'_{H_2} \qquad (28)$$

Inert sweep side:
$$J''_V = k_{r,O} C''_{O_O^x} C''^2_{h^\bullet} - k_{f,O} C''^{0.5}_{O_2} C''_V \qquad (29)$$

Fuel sweep side:
$$J''_V = k_{f,H} C''_{O_O^x} C''^2_{h^\bullet} C''_{H_2} - k_{r,H} C''_{H_2O} C''_V \qquad (30)$$

Here, J'_V and J''_V are the absolute values of oxygen vacancy fluxes at feed and sweep side surfaces, respectively; C'_i and C''_i are the concentrations of species i on the feed side and sweep side, respectively.

To simplify the flux equations, we neglect the reverse reactions on the water feed side and the hydrogen sweep side, as the reverse rates are low compared with the forward reaction rate. Similar assumptions have been made in literature for heterogeneous reactions with MIEC membranes [26]. Besides, electron conductivity of a typical perovskite material is high so that the electron hole concentration is assumed to be constant across the membrane. Therefore, the vacancy flux is viewed as zero-order in electron hole concentrations, $C'^2_{h^\bullet}$ and $C''^2_{h^\bullet}$. [32,33,36] Additionally, the sum of lattice oxygen concentration $C_{O_O^x}$ and oxygen vacancy concentration C_V is the total oxygen site concentration in the LCF-91 lattice,

$$C_O = C_{O_O^x} + C_V \qquad (31)$$

The concentration of oxygen sites in the lattice is,

$$C_O = \frac{3}{V_M} = 0.0825 \quad mol/cm^3 \qquad (32)$$

where V_M is the molar volume of LCF, $V_M = 36.37$ cm³/mol.

With the above assumptions, the vacancy fluxes are simplified as:

Oxygen feed side:
$$J'_V = k_{f,O} C'^{0.5}_{O_2} C'_V - \tilde{k}_{r,O} \left(C_O - C'_V \right) \qquad (33)$$

Water feed side:
$$J'_V = k_{r,H} C'_{H_2O} C'_V \qquad (34)$$

Inert sweep side:
$$J''_V = \tilde{k}_{r,O} \left(C_O - C''_V \right) - k_{f,O} C''^{0.5}_{O_2} C''_V \qquad (35)$$

Fuel sweep side:
$$J''_V = \tilde{k}_{f,H} C''_{H_2} \left(C_O - C''_V \right) \qquad (36)$$

Here, $\tilde{k}_{r,O}$ and $\tilde{k}_{f,H}$ are the new reaction constants after lumping the electron hole concentration.

Additionally, the oxygen vacancy diffusion flux can be calculated from the bulk diffusion. For the vacancy diffusion in the bulk due to a chemical potential gradient $\nabla \mu_V$, the Nernst-Planck equation gives

$$J_V = -\frac{\sigma_V}{\left(z_V F \right)^2} \nabla \mu_V \qquad (37)$$

where σ_V is the conductivity of oxygen vacancy in the membrane, z_V is the charge of oxygen vacancy and F is Faraday constant.

The conductivity of oxygen vacancy is

$$\sigma_V = \frac{\left(z_V F \right)^2}{RT} C_V D_V \qquad (38)$$

where C_V is oxygen vacancy concentration, D_V is the diffusivity of oxygen vacancy, R is universal gas constant and T is the temperature.

On the other hand, the chemical potential gradient of oxygen vacancy across of the membrane is

$$\nabla \mu_V = \frac{\partial \left(RT \ln \left(C_V \right) \right)}{\partial y} = \frac{RT}{C_V} \frac{\partial \left(C_V \right)}{\partial y} \qquad (39)$$

Combining (37), (38) and (39), we derive the oxygen vacancy diffusion rate in the bulk as

$$J_V = -D_V \frac{\partial C_V}{\partial y} = D_V \frac{C''_V - C'_V}{t} \qquad (40)$$

where t is the thickness of the membrane.

By equating the oxygen vacancy flux on the feed side surface (33) or (34), through the bulk (40) and on the sweep side surface (35) or (36), the flux equation can be expressed in the form of the potential difference over the sum of three resistances as

$$J_V = \frac{\Delta P}{R_f + R_b + R_s} \qquad (41)$$

where ΔP is the potential difference, R_f, R_b and R_s are the resistances of the feed side surface reaction, the bulk diffusion and the sweep side surface reaction, respectively. Details of the expressions are given in Table 2.

5.2 Reaction kinetics

In addition to the water thermolysis experiments shown in previous sections, we also experimented with the cases where air serves as the oxygen source with either inert or reactive sweep gases. Here, we present the oxygen fluxes through 0.9-mm thick LCF-91 membranes at the 990 °C, the same as the water thermolysis experiments. Helium sweep gas flow rates vary from 20 – 500 sccm. As shown in Figure 8, the oxygen fluxes increase with increasing helium flow rate. Similar phenomena were also found for other perovskite membranes [32,37]. Additionally, when the helium sweep gas flow rate increases from 20 to 500 sccm, the oxygen partial pressure at the outlet of the sweep chamber decreases by an order of magnitude, i.e., from 0.4 to 0.077 kPa.

Table 2 Resistance network for various oxygen sources and sweep side mechanisms on an MIEC oxygen permeable membrane

Oxygen source	Air	Air	Water vapor	Water vapor
Sweep side mechanism	Inert sweep	H_2 reactive	Inert sweep	H_2 reactive
Feed side reaction rate	(23)	(23)	(24)	(24)
Sweep side reaction rate	(25)	(26)	(25)	(26)
Potential gradient, ΔP	$\left(\dfrac{\tilde{k}_{r,o}C_O}{\tilde{k}_{r,o}+k_{f,o}C'^{0.5}_{O_2}} - \dfrac{\tilde{k}_{r,o}C_O}{\tilde{k}_{r,o}+k_{f,o}C'^{0.5}_{O_2}} \right)$	$C_O - \dfrac{\tilde{k}_{r,o}C_O}{\tilde{k}_{r,o}+k_{f,o}C'^{0.5}_{O_2}}$	$\dfrac{\tilde{k}_{r,o}C_O}{\tilde{k}_{r,o}+k_{f,o}C'^{0.5}_{O_2}}$	C_O
Surface reaction resistance (feed side), R_f	$\dfrac{1}{\tilde{k}_{r,o}+k_{f,o}C'^{0.5}_{O_2}}$	$\dfrac{1}{\tilde{k}_{r,o}+k_{f,o}C'^{0.5}_{O_2}}$	$\dfrac{1}{k_{r,H}C'_{H_2O}}$	$\dfrac{1}{k_{r,H}C'_{H_2O}}$
Bulk resistance, R_b	$\dfrac{t}{D_V}$	$\dfrac{t}{D_V}$	$\dfrac{t}{D_V}$	$\dfrac{t}{D_V}$
Surface reaction resistance (sweep side), R_s	$\dfrac{1}{\tilde{k}_{r,o}+k_{f,o}C''^{0.5}_{O_2}}$	$\dfrac{1}{\tilde{k}_{f,H}C''_{H_2}}$	$\dfrac{1}{\tilde{k}_{r,o}+k_{f,o}C''^{0.5}_{O_2}}$	$\dfrac{1}{\tilde{k}_{f,H}C''_{H_2}}$

When hydrogen and helium mixture acts as the sweep gas, the oxygen fluxes are shown in Figure 9. The total flow rate of the sweep mixture is fixed at 500 sccm while the hydrogen concentration changes. The oxygen fluxes calculated from the feed side (Equation(18)) or from the sweep side (Equation(20)) are the same. Thus, material balance inside the reactor is satisfied, which also means that all oxygen permeated through the membrane reacts with the hydrogen in the sweep chamber. Figure 9 (a) shows that the oxygen fluxes increase with hydrogen concentrations in the sweep stream. The oxygen flux with 15 vol% hydrogen in the sweep side is 5 times higher than that in the inert sweep case. The consumption ratio of hydrogen in the sweep gas is shown in Figure 9 (b). The consumption ratio is as low as 2-6%, and it decreases at higher hydrogen concentration on the sweep side. Beyond 3% hydrogen concentration, the consumption ratio stays constant around 2%. The short residence time of the sweep mixture and the limited availability of oxygen may be the reasons for the low hydrogen consumption ratio.
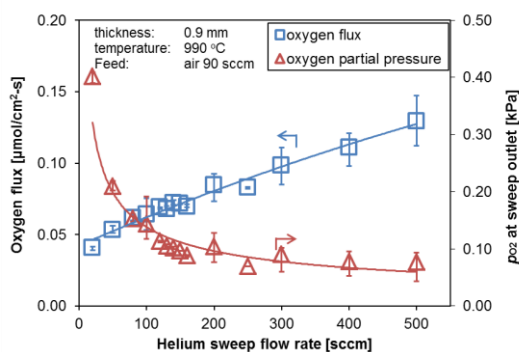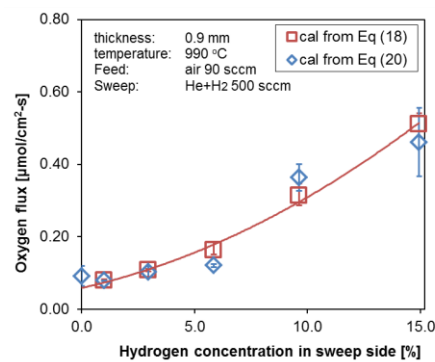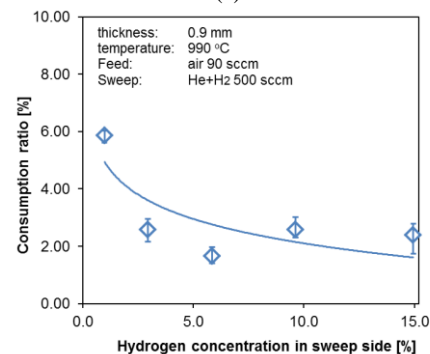

Figure 8 For the 0.9 mm LCF-91 membrane at 990 °C, oxygen flux increases but the values of oxygen partial pressure on the sweep side drops at higher sweep flow rate

Based on the data of the four cases, i.e., water feed-inert sweep, water feed-fuel sweep, air feed-inert sweep and air feed-fuel sweep, the reaction rate constants for the oxygen incorporation/dissociation (Reaction (23)) and hydrogen-oxygen surface reactions (Reaction (26)) are derived by a least squares fitting. The values of $k_{f,o}$ and $\tilde{k}_{r,o}$ for Reaction (23) are first fitted using air feed-inert sweep data. Then the values of $\tilde{k}_{f,H}$ and $k_{r,H}$ for Reaction (26) are fitted using the air feed-fuel sweep, water feed-inert sweep and water feed-fuel sweep data. The higher oxygen flux data are manually weighted in order to have better fitting at larger values. The values of the rate constants are shown in Table 3. These rate constants are in similar orders of magnitude with those values in literature under similar conditions [26,38]. The vacancy bulk diffusivity, D_v in LCF-91 was derived from separate transient dilatometry studies and fitted in Arrhenius relation [38]; the D_v value at 990 °C is shown in Table 3.

(a)

(b)

Figure 9 Oxygen flux through a 0.9 mm LCF-91 membrane at 990 °C increases with hydrogen concentration in the sweep chamber. Air flows on the feed side at 90 sccm, and helium and hydrogen mixture flows on the sweep side at a total flow rate of 500 sccm. (a) Oxygen fluxes and (b) hydrogen consumption ratio dependence are shown

Table 3 Reaction kinetic parameters for oxygen surface reactions and bulk diffusion at 990 $^{\circ}$C for LCF-91 membrane

|	Parameter		value	Literature values
1 bulk diffusivity	D_v	[cm^2/s]	1.7 E-05 [38]	/
2 oxygen surface reaction	$k_{f,O}$	[cm$^{2.5}$/mol$^{0.5}$-s]	1.9	0.193 * [38]
Reaction (23)	$\widetilde{k}_{r,O}$	[cm/s]	3.15 E-6	6.487E-7 * [38]
3 water surface reaction	$\widetilde{k}_{f,H}$	[cm^4/mol-s]	1.4 E-1	/
Reaction (26)	$k_{r,H}$	[cm^4/mol-s]	6.2	5.047 ** [26]
* Oxygen incorporation/dissociation with air feed-CO$_2$ sweep through LCF-91 membranes;				
** Hydrogen oxidation at sweep side with air feed-fuel sweep through LSF-73 membranes [39].				
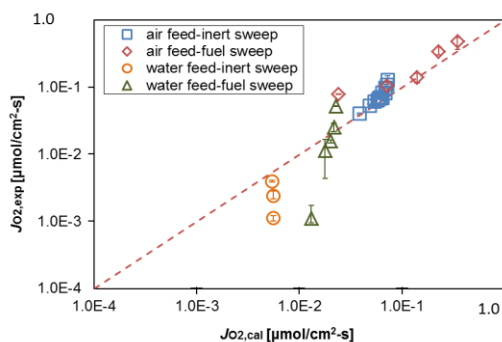
Figure 10 The comparison between the experimental and the calculated oxygen fluxes using the fitted reaction kinetic parameter shown in Table 3. The data correspond to the previous figures: water feed-fuel sweep (Figure 6), air feed-inert sweep (Figure 8), air feed-fuel sweep (Figure 9) and water feed-inert sweep (Figure 4).

Using the reaction rate constants obtained, we calculated the oxygen fluxes with the three-resistance model in Equation (41) and Table 2, and compared the calculated values with the experimental values, which are shown in Figure 10. At high oxygen flux values, the calculated and experimental oxygen fluxes match well; yet at lower J_{O2} values, there are larger discrepancies. The discrepancy may come from the fact that bulk measurements are used in this study to estimate the local conditions at membrane surface. As shown by Hong et al. [33], the difference between the bulk and local values, especially on the sweep side, may lead to different kinetic parameter fittings. And when the oxygen fluxes are low, the local values differ from the bulk to a larger extend. Additionally, the one-step heterogeneous mechanism may not be able to capture the limiting sub-steps under various operating conditions, which may also result in the difference between the calculated and experimental values. Yet Figure 10 shows some good matches between the calculated and experimental oxygen fluxes. In the following discussion, we use these reaction rate constants in Table 3 to compare the oxygen permeation mechanism with different oxygen sources and sweep gases.

6. Comparison between different oxygen sources

In this section, we compare the mechanisms for oxygen permeation through an MIEC perovskite membrane with water or air being the oxygen sources and inert or reactive gases being the sweep gas. Based on the resistance model in Equation (41) and the reaction kinetic parameters in Table 3, limiting steps are identified under various operating conditions. A summary of the comparison between resistances R_f, R_b and R_s is listed in Table 4.
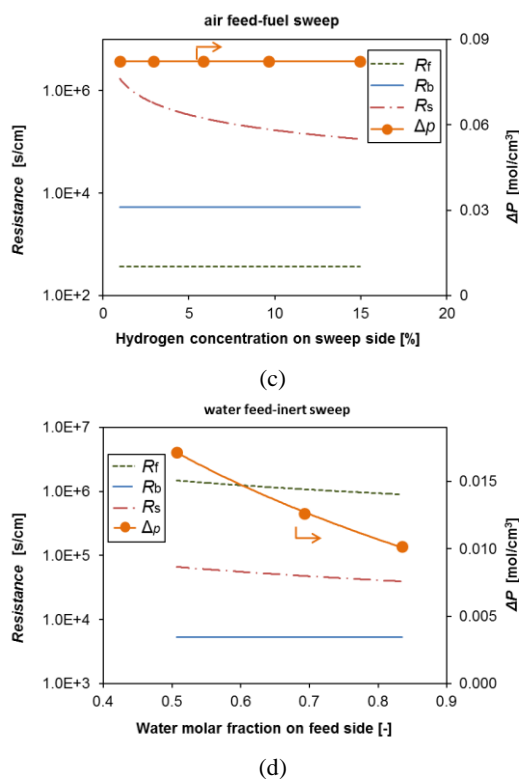

(a)

(b)

(c)

(d)
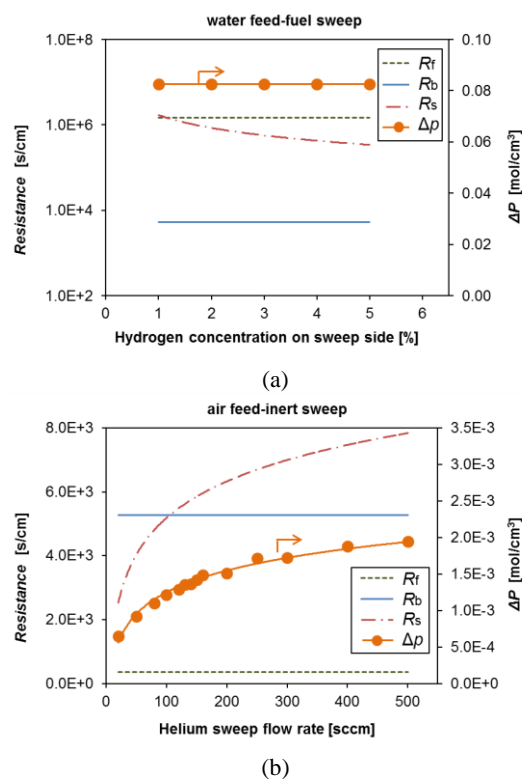
Figure 11 Resistances and potential difference in the four cases: (a) water feed-fuel sweep (Figure 6), (b) air feed-inert sweep (Figure 8), (c) air feed-fuel sweep (Figure 9) and (d) water feed-inert sweep (Figure 4). Experimental conditions are depicted in the associated figures.

6.1 Water feed-fuel sweep

First, we discuss the case when the oxygen source is water vapor and the sweep gas is fuel. In this case, the surface reactions on the feed and sweep side surfaces are the forward and reverse water thermolysis (Reactions (24) and (26)), respectively. As shown in Figure 6 (a), fuel addition in the sweep side enhances the water thermolysis rate. Referring to Table 2, the oxygen flux is

$$J_{O_2} = \frac{1}{2} J_V = \frac{1}{2} \cdot \frac{C_O}{\dfrac{1}{k_{r,H} C'_{H_2O}} + \dfrac{t}{D_v} + \dfrac{1}{\tilde{k}_{f,H} C''_{H_2}}} \, . \tag{42}$$

The resistances and the potential difference are shown in Figure 11 (a). The potential difference, the bulk resistance and the feed side surface reaction resistance remain constant by construction. As the hydrogen concentration on the sweep side increases, the sweep side surface reaction resistance drops. The surface reaction resistances on both sides are on the same order of magnitude, and are larger than the bulk diffusion resistance. Therefore, both the surface reactions are the limiting steps for this 0.9-mm thick membrane, when 50 vol% water is the oxygen source and hydrogen-helium mixture (1 – 5 vol% H_2) the sweep gas.

Table 4 Summary of the importance of the resistances for oxygen permeation through a 0.9-mm thick LCF-91 membrane at 990 °C

Oxygen source		Air	Air	Water vapor	Water vapor
Sweep gas		Helium	1-15 vol% H_2 + helium	helium	1-5 vol% H_2 + helium
Resistance comparison	R_f	3	3	1	1
	R_b	1	2	3	3
	R_s	1	1	2	1
1 is the largest, and 3 is the smallest.					

6.2 Air feed-inert sweep

In the case where oxygen source is air and the sweep gas is inert, only the oxygen surface incorporation/dissociation, i.e., Reaction (23) is involved. In this case, the oxygen flux is:

$$J_{O_2} = \frac{1}{2} J_V = \frac{1}{2} \cdot \frac{\left(\dfrac{\tilde{k}_{r,o} C_O}{\tilde{k}_{r,o} + k_{f,o} C'^{0.5}_{O_2}} - \dfrac{\tilde{k}_{r,o} C_O}{\tilde{k}_{r,o} + k_{f,o} C''^{0.5}_{O_2}} \right)}{\dfrac{1}{\tilde{k}_{r,o} + k_{f,o} C'^{0.5}_{O_2}} + \dfrac{t}{D_v} + \dfrac{1}{\tilde{k}_{r,o} + k_{f,o} C''^{0.5}_{O_2}}} \, . \tag{43}$$

As in Figure 11 (b), the bulk resistance and the feed side surface reaction resistance remain constant by construction. Both the potential difference ΔP and the sweep side surface reaction resistance R_s increase with helium sweep flow rate. The growth of ΔP and R_s are associated with the drop in oxygen concentration on the sweep side when helium sweep rate increases (see Figure 8). However, as ΔP grows faster than R_s, the overall oxygen flux in this case increases at higher helium flow rate.

Additionally, as shown in Figure 11 (b), the feed side surface reaction resistance is the lowest among the three resistances. Yet there are two regimes that can be identified by comparing the bulk resistance and sweep side surface reaction resistance for this 0.9-mm thick LCF-91 membrane at 990 °C. At low flow rate with the helium sweep rate lower than 150 sccm, the bulk resistance dominates; but at high flow rate regime, the sweep side surface reaction resistance dominates.

6.3 Air feed-fuel sweep

The two cases discussed above involve one type of surface reactions only, either oxygen incorporation/dissociation or forward/reverse water thermolysis. Yet in the air feed-fuel sweep case, oxygen incorporation/dissociation occurs on the feed side while reverse water thermolysis (or hydrogen oxidation) takes place on the sweep side.

From Table 2, the overall oxygen flux is,

$$J_{O_2} = \frac{1}{2} J_V = \frac{1}{2} \cdot \frac{\left(C_O - \frac{\tilde{k}_{r,O} C_O}{\tilde{k}_{r,O} + k_{f,O} C_{O_2}^{0.5}} \right)}{\frac{1}{\tilde{k}_{r,O} + k_{f,O} C_{O_2}^{0.5}} + \frac{t}{D_v} + \frac{1}{\tilde{k}_{f,H} C_{H_2}^{''}}} \cdot \quad (44)$$

As shown in Figure 11 (c), the potential difference, the feed side surface reaction resistances and the bulk diffusion resistance remain constant by construction. And R_f is the lowest among the three resistances which is the same with that in air feed-inert sweep case. Yet R_s decreases at higher hydrogen concentration. Therefore, the enhancement of oxygen flux by adding hydrogen on the sweep side is mainly due to the decrease of sweep side surface reaction resistance.

6.4 Water feed-inert sweep

Another case that involves both oxygen incorporation/dissociation and forward/reverse water thermolysis is the one with water as the feed gas and helium as the sweep gas. Results in previous section show that the oxygen flux is dependent on the mixture flow rate and water concentration on the feed side, but independent on the helium sweep flow rate.

From Table 2, the oxygen flux in this case is

$$J_{O_2} = \frac{1}{2} J_V = \frac{1}{2} \cdot \frac{\left(\frac{\tilde{k}_{r,O} C_O}{\tilde{k}_{r,O} + k_{f,O} C_{O_2}^{''0.5}} \right)}{\frac{1}{k_{r,H} C_{H_2O}^{'}} + \frac{t}{D_v} + \frac{1}{\tilde{k}_{r,O} + k_{f,O} C_{O_2}^{''0.5}}} \cdot \quad (45)$$

Figure 11 (d) shows the three resistances and potential difference corresponding to the case in Figure 4 where the feed side water concentration changes. For this 0.9-mm thick membrane, R_b is the lowest among the three resistances and R_f is the highest. As R_f is around two-order of magnitude higher than R_s, the oxygen permeation process is limited by the feed side surface reaction rate. This explains why the water thermolysis ratio and the corresponding hydrogen yield depend on the flow rate and water concentration on the feed side rather than the sweep gas flow rate. Besides, with increasing water concentration on the feed side, the feed and sweep side surface reaction resistances as well as the potential difference drops.

6.5 Comparisons between different conditions

The resistances to the oxygen permeation through the 0.9-mm thick LCF-91 membrane with various oxygen sources and sweep gases are summarized in Table 4. For the 0.9-mm thick membrane, the bulk diffusion is the limiting step in the air feed-water sweep case; in other cases, the bulk resistance, R_b, is orders-of-magnitude lower than the highest resistance.

In the air feed cases, the feed side surface reaction resistance, R_f, can be neglected with either inert or reactive sweep gas; yet the sweep side surface reaction resistance R_s plays the important role. In the air feed-inert sweep case (Figure 11 (b)), R_s is in the same order of magnitude with R_b; in the air feed-fuel

sweep case (Figure 11 (c)), R_s is the highest but drops and approaches the values of R_b at higher hydrogen concentration. Therefore, apart from utilizing thinner LCF-91 membranes, improvements should be applied on the sweep side such as increasing surface area and applying catalysts to enhance oxygen dissociation or fuel oxidation rates, and hence, to increase the overall oxygen flux.
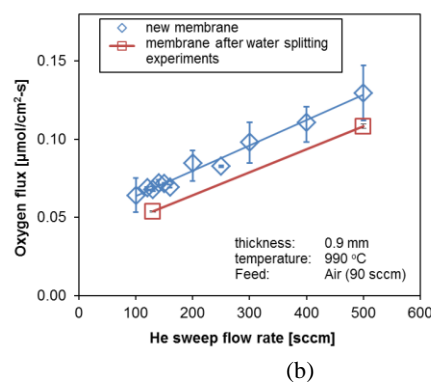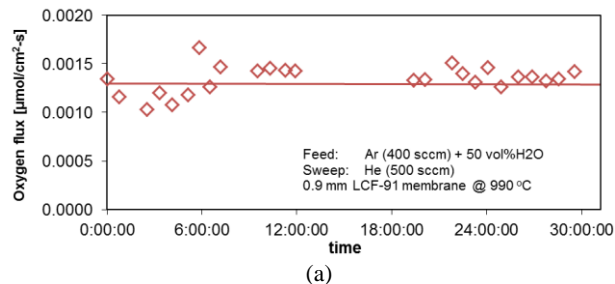

(a)

(b)

Figure 12 Long term stability studies of membrane using water as oxygen source. (a) Oxygen flux (water thermolysis rate) keeps constant for 30 hours of experiments. (b) After 60 hours of exposure to water vapor on the feed side, the oxygen flux of air separation for this 0.9 mm LCF-91 membrane didn't degrade.

On the other hand, in the water feed cases, R_f dominates no matter when the sweep gas is inert or reactive. Yet when the sweep gas contains 1-5 vol% hydrogen, R_s is lower but in similar order of magnitude with R_f. Therefore, for the water thermolysis reactor with LCF-91 membrane, if we try to incorporate oxygen production on the sweep side, where the sweep is inert or vacuum, improvements should be applied on the feed side. Yet if reactions such as syngas production are designed on the sweep side, depending on the fuel concentration, improvements on the feed and the sweep sides might both be necessary.

7. Membrane stability under water vapor conditions

7.1 Long term stability test

A long term stability test was carried out for the water vapor as oxygen source in order to verify that this LCF-91 oxygen permeable perovskite membrane is stable in the experimental environments in this study. Results are shown in Figure 12 (a), which shows stable oxygen fluxes through the membrane were

maintained over a 30-hour period. After 60 hours of exposure to water vapor at the feed side, the oxygen source was switched to air and oxygen permeation rate was measured. As shown in Figure 12 (b), the oxygen fluxes from air are within the error bar, which means that exposing to high concentration of water vapor (50.7 to 83.5 vol%) on the feed side didn't deteriorate the oxygen permeation performances of the membrane.

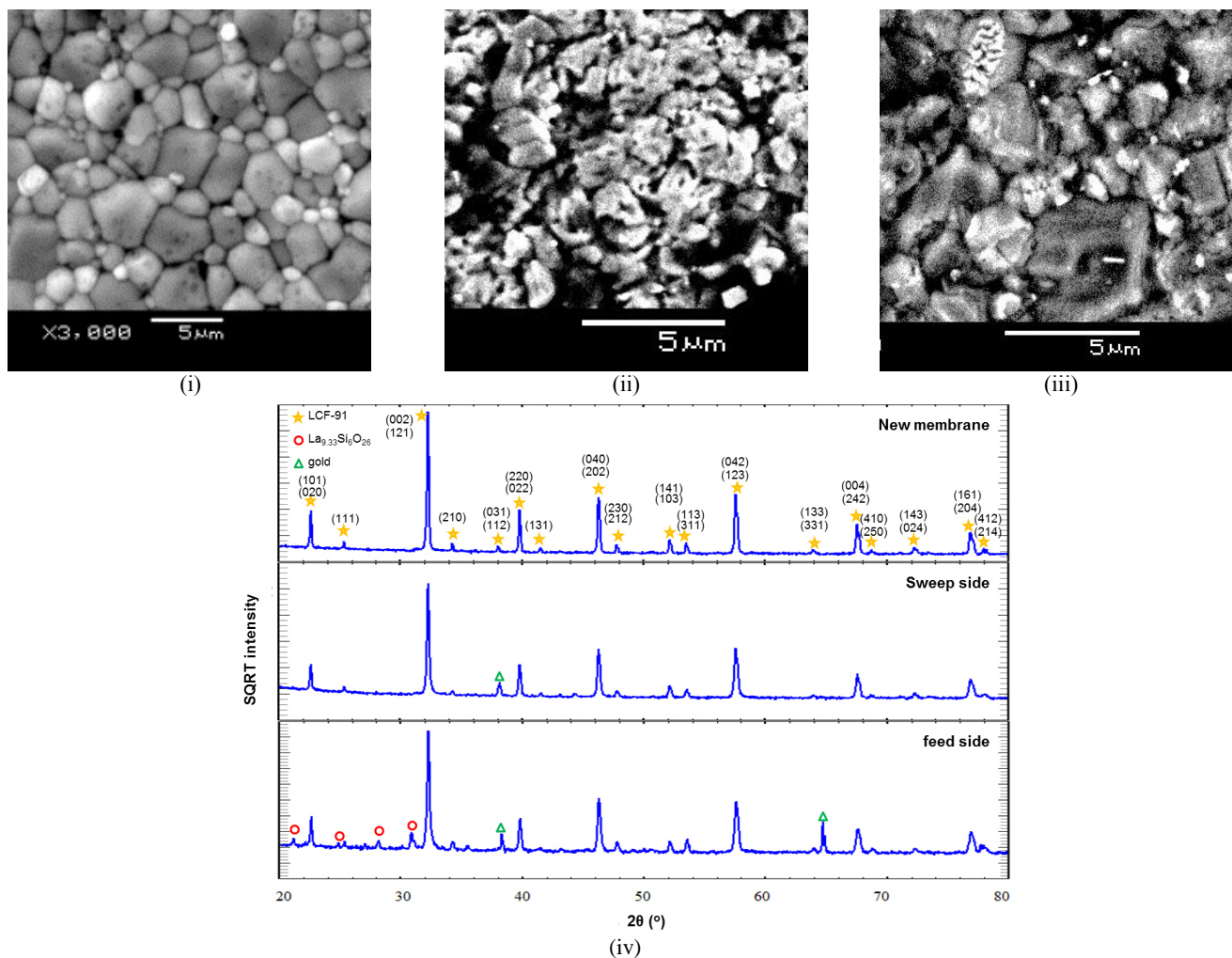(i)   (ii)   (iii)

(iv)

Figure 13 Characterization of LCF-91 membranes before and after experiments: SEM images of (i) a new membrane, (ii) sweep side and (iii) feed side of a used membrane and (iv) XRD profiles (diffraction plane numbers of LCF-91 are listed by the XRD peaks.)

7.2 Membrane morphology and lattice structure

The characteristics of the membrane bulk and surface were examined by the SEM and XRD to study the surface morphology and lattice structures. Figure 13 (i) – (iii) shows the SEM images of the LCF-91 membrane before and after oxygen permeation experiments with air or water vapor as the oxygen source. The membrane before experiments shows very fine grains with sizes ranging from 0.5 -5 μm. Yet after the experiments, the surface morphologies change on both feed and sweep sides. On the sweep side where surface reduction reaction occurs, the grains became coarse with smaller sizes; the grain boundaries are harder to identify. On the feed side where oxygen incorporates into the membrane surface, smaller particles appear on the surfaces and the grain boundaries are obscure.

Figure 13 (iv) compares the XRD patterns of the new membranes and the used membrane surfaces. The sweep side shows very good LCF-91 peaks, while the feed side shows lanthanum silicate impurity peaks. The source of the silicon on the surface is likely to be the silica gel desiccant on the downstream of the reactor outlet used to dry the gas samples before entering the gas chromatographer. Despite the changes on the morphologies as well as the silica impurities, the oxygen permeation performances of the membrane didn't change during the experiments.

Conclusions

Mixed ionic and electronic conducting membranes have the capabilities of permeating oxygen selectively. Oxygen separation from air by MIEC membranes has been studied extensively in literature, but only a few studies present enhanced water thermolysis by integration with an MIEC membrane reactor. In this work, we present the enhanced water thermolysis characteristics through 0.9 mm thick LCF-91 membranes in a lab-scale button-cell reactor with inert or reactive sweep gas. As oxygen flux is a good illustrator for water thermolysis rate, we study the oxygen fluxes under various operating conditions such as the gas flow rates and species concentrations on feed or sweep sides. Oxygen flux from air separation is also studied, and three-resistance models for water thermolysis and air separation are compared. Results show the following:

(1) The limiting step of oxygen permeation process is different depending on both the oxygen source and the sweep gas. A summary is shown in Table 4, comparing the resistances of the four cases studied in this paper.

(2) Water thermolysis rate is enhanced by the LCF-91 membranes compared to the homogeneous case. With inert sweep gas, the limiting step is water heterogeneous thermolysis reaction on the feed side. The oxygen flux grows with increasing feed flow rate and water concentration on the feed side, but it is independent of the helium sweep gas flow rate. Yet when the sweep gas is reactive, i.e. hydrogen and helium mixtures, the limiting steps are the surface reactions on both the feed and sweep sides. The water thermolysis rate or the corresponding hydrogen yield is further enhanced with increasing hydrogen concentration, as the sweep side surface reaction resistance drops.

(3) When air is the oxygen source, the limiting steps are different. The feed side reaction resistance can be neglected in both the inert and reactive sweep cases. Yet the sweep side surface reaction resistance plays an important role in both sweep cases. Increasing sweep flow rate of helium sweep gas or adding fuel on the sweep side can increase the oxygen fluxes.

(4) Long term stability tests were carried out and there is no degradation of oxygen flux with either air or water vapor as the oxygen sources. Yet surface morphologies changes as well as impurities were identified by SEM and XRD results.

Acknowledgements

Notes and references

[a] Department of Mechanical Engineering, Massachusetts Institute of Technology, 77 Massachusetts Avenue, Cambridge, MA 02139, USA.
[b] Department of Mechanical Engineering, University of British Columbia, 2054-6250 Applied Science Lane, Vancouver, BC, Canada.
†Email address: xywu@mit.edu (X.Y. Wu), ghoniem@mit.edu (A.F. Ghoniem).

1. IEA, *World Energy Outlook*, 2012.
2. A. F. Ghoniem, *Prog. Energy Combust. Sci.*, 2011, **37**, 15-51.
3. S. D. Ebbesen, S. H. Jensen, A. Hauch and M. B. Mogensen, *Chem. Rev.*, 2014, **114**, 10697-10734.
4. M. A. Laguna-Bercero, *J. Power Sources*, 2012, **203**, 4-16.
5. M. Carmo, D. L. Fritz, J. Merge and D. Stolten, *Int. J. Hydrogen Energy*, 2013, **38**, 4901-4934.
6. T. Ramsden and M. Ruth, Current (2010) Hydogen Production from Central Grid Electrolysis, http://www.hydrogen.energy.gov/h2a_production.html.
7. G. Saur, T. Ramsden, B. James and W. Colella, Current (2010) Hydrogen Production from Central Grid PEM Electrolysis, http://www.hydrogen.energy.gov/h2a_production.html.
8. M. Rutkowski, Current (2010) Hydrogen from Natural Gas without CO_2 Capture and Sequestration, http://www.hydrogen.energy.gov/h2a_production.html.
9. U. Balachandran, *Int. J. Hydrogen Energy*, 2004, **29**, 291-296.
10. A. Evdou, L. Nalbandian and V. Zaspalis, *J. Membr. Sci.*, 2008, **325**, 704-711.
11. R. V. Franca, A. Thursfield and I. S. Metcalfe, *J. Membr. Sci.*, 2012, **389**, 173-181.
12. S. J. Song, J. H. Moon, H. W. Ryu, T. H. Lee, S. E. Dorris and U. Balachandran, *J. Ceramic Process. Res.*, 2008, **9**, 123-125.
13. N. Zhu, X. Dong, Z. Liu, G. Zhang, W. Jin and N. Xu, *Chem. Commun.*, 2012, **48**, 7137-7139.
14. H. Wang, S. Gopalan and U. B. Pal, *Electrochim. Acta*, 2011, **56**, 6989-6996.
15. H. Jiang, H. Wang, F. Liang, S. Werth, S. Schirrmeister, T. Schiestel and J. Caro, *Catal. Today*, 2010, **156**, 187-190.
16. L. Chang, MS Thesis, Massachusetts Institute of Technology, 2013.
17. J. Sunarso, S. Baumann, J. M. Serra, W. A. Meulenberg, S. Liu, Y. S. Lin and J. C. Diniz da Costa, *J. Membr. Sci.*, 2008, **320**, 13-41.
18. A. Thursfield, A. Murugan, R. Franca and I. S. Metcalfe, *Energy Environ. Sci.*, 2012, **5**, 7421 - 7459.
19. Y. Liu, X. Tan and K. Li, *Cat. Rev.*, 2006, **48**, 145-198.
20. S. Aasland, I. L. Tangen, K. Wiik and R. Ødegård, *Solid State Ionics*, 2000, **135**, 713-717.
21. Q. Liao, Y. Wang, Y. Chen, Y. Wei and H. Wang, *J. Membr. Sci.*, 2014, **468**, 184-191.
22. C. Y. Park, T. H. Lee, S. E. Dorris, Y. Lu and U. Balachandran, *Int. J. Hydrogen Energy*, 2011, **36**, 9345-9354.
23. C. Y. Park, T. H. Lee, S. E. Dorris and U. Balachandran, *ECS Trans.*, 2008, **13**, 393-403.
24. K. Foy and J. McGovern, Comparison of Ion Transport Membranes, Virginia, 2005.
25. M. Carolan, C. Chen, J. Chen, C. Miller, E. Minford and W. Waldron, *ECS Trans.*, 2008, **13**, 319-325.

Physical Chemistry Chemical Physics Accepted Manuscript

26. J. Hong, P. Kirchen and A. F. Ghoniem, *J. Membr. Sci.*, 2013, **445**, 96-106.

27. Y. Q. Liang, N. L. Di and Z. H. Cheng, *Phys. Rev. B*, 2005, **72**, 134416.

28. A. N. Nadeev, S. V. Tsybulya, E. Y. Gerasimov, N. A. Kulikovskaya and L. A. Isupova, *J. Struct. Chem.*, 2010, **51**, 891-897.

29. R. Shannon, *Acta Crystallogr. Sect. A*, 1976, **32**, 751-767.

30. D. G. Goodwin, Cantera, http://www.aresinstitute.org/Cantera/cantera-cxx.pdf.

31. G. P. Smith, D. M. Golden, M. Frenklach, N. W. Moriarty, B. Eiteneer, M. Goldenberg, C. T. Bowman, R. K. Hanson, S. Song, W. C. Gardiner, V. V. Lissianski and Z. Qin, GRI-Mech 3.0, http://www.me.berkeley.edu/gri_mech/.

32. S. J. Xu and W. J. Thomson, *Chem. Eng. Sci.*, 1999, **54**, 3839-3850.

33. J. Hong, P. Kirchen and A. F. Ghoniem, *J. Membr. Sci.*, 2012, **407-408**, 71-85.

34. Z. Wang, N. Yang, B. Meng, X. Tan and K. Li, *Ind. Eng. Chem. Res.*, 2008, **48**, 510-516.

35. J. E. ten Elshof, H. J. M. Bouwmeester and H. Verweij, *Solid State Ionics*, 1995, **81**, 97-109.

36. L. Qiu, T. H. Lee, L. M. Liu, Y. L. Yang and A. J. Jacobson, *Solid State Ionics*, 1995, **76**, 321-329.

37. F. T. Akin and J. Y. S. Lin, *J. Membr. Sci.*, 2004, **231**, 133-146.

38. A. Hunt, G. Dimitrakopoulos, P. Kirchen and A. F. Ghoniem, *J. Membr. Sci.*, 2014, **468**, 62-72.

39. X. Tan, L. Shi, G. Hao, B. Meng and S. Liu, *Sep. Purif. Technol.*, 2012, **96**, 89-97.

Physical Chemistry Chemical Physics Accepted Manuscript